NANO · MICRO

small

Hydration

Day 1 Day 2 Day 3 Day 4 Day 5 Day 6 Day 7

Wireless, Battery-Free Epidermal Electronics for Continuous, Quantitative, Multimodal Thermal Characterization of Skin

Siddharth R. Krishnan, Chun-Ju Su, Zhaoqian Xie, Manish Patel, Surabhi R. Madhvapathy, Yeshou Xu, Juliet Freudman, Barry Ng, Seung Yun Heo, Heling Wang, Tyler R. Ray, John Leshock, Izabela Stankiewicz, Xue Feng, Yonggang Huang, Philipp Gutruf,* and John A. Rogers*

Precise, quantitative measurements of the thermal properties of human skin can yield insights into thermoregulatory function, hydration, blood perfusion, wound healing, and other parameters of clinical interest. The need for wired power supply systems and data communication hardware limits, however, practical applicability of existing devices designed for measurements of this type. Here, a set of advanced materials, mechanics designs, integration schemes, and wireless circuits is reported as the basis for wireless, battery-free sensors that softly interface to the skin to enable precise measurements of its temperature and thermal transport properties. Calibration processes connect these parameters to the hydration state of the skin, the dynamics of near-surface flow through blood vessels and implanted catheters, and to recovery processes following trauma. Systematic engineering studies yield quantitative metrics in precision and reliability in real-world conditions. Evaluations on five human subjects demonstrate the capabilities in measurements of skin hydration and injury, including examples of continuous wear and monitoring over a period of 1 week, without disrupting natural daily activities.

S. R. Krishnan, Prof. J. A. Rogers
Department of Materials Science and Engineering
Frederick Seitz Materials Research Laboratory
University of Illinois at Urbana-Champaign
Urbana, IL 61801, USA
E-mail: jrogers@northwestern.edu

S. R. Krishnan
Simpson Querrey Institute for BioNanotechnology
Center for Bio-Integrated Electronics
Northwestern University
Evanston, IL 60208, USA

C.-J. Su, M. Patel, S. R. Madhvapathy, B. Ng, Dr. T. R. Ray
Department of Materials Science and Engineering
Simpson Querrey Institute for BioNanotechnology
Center for Bio-Integrated Electronics
Northwestern University
Evanston, IL 60208, USA

Dr. Z. Xie, Y. Xu, Dr. H. Wang
Department of Civil and Environmental Engineering
Mechanical Engineering
Materials Science and Engineering
Northwestern University
Evanston, IL 60208, USA

Y. Xu
Key Laboratory of C&PC Structures of the Ministry of Education
Southeast University
Nanjing 210096, China

J. Freudman, S. Y. Heo, J. Leshock, I. Stankiewicz
Department of Biomedical Engineering
Simpson Querrey Institute for BioNanotechnology
Center for Bio-Integrated Electronics
Northwestern University
Evanston, IL 60208, USA

Prof. X. Feng
AML
Department of Engineering Mechanics
Center for Mechanics and Materials
Tsinghua University
Beijing 100084, China

Prof. Y. Huang
Department of Civil and Environmental Engineering
Mechanical Engineering
Materials Science and Engineering
Center of Bio-integrated electronics
Northwestern University
Evanston, IL 60208, USA

Prof. P. Gutruf
Department of Biomedical Engineering
University of Arizona
Tucson, AZ 85721, USA
E-mail: pgutruf@email.arizona.edu

Prof. J. A. Rogers
Department of Materials Science and Engineering
Biomedical Engineering, Chemistry
Mechanical Engineering
Electrical Engineering and Computer Science
and Neurological Surgery
McCormick School of Engineering
and Feinberg School of Medicine
Simpson Querrey Institute for BioNanotechnology
Center for Bio-Integrated Electronics
Northwestern University
Evanston, IL 60208, USA

**ADVANCED
SCIENCE NEWS**
www.advancedsciencenews.com

NANO · MICRO
small
www.small-journal.com

1. Introduction

Skin, as the largest organ of the body, plays a critical role in homeostasis and thermoregulation; it also determines external appearance and acts as a barrier to airborne toxins, preventing the diffusion of pathogens, pollutants and particulates.[1–4] Conventional means for monitoring the biophysical properties of skin require either paste-on sensors with complex wiring schemes,[5] visual inspection from trained medical professionals, or handheld probes that involve precise calibration for pressure at the contacting interface.[6,7] For applications in continuous monitoring and/or measurements in the home, such approaches fail to offer desired levels of convenience, comfort, ease of use, reliability, or accuracy. Recent advances in materials science and mechanical engineering form the basis of classes of electronic devices that are soft, thin, stretchable, and skin like in their physical properties. Such technologies sometimes collectively referred to as "epidermal electronics," can produce clinical-quality data streams in a range of settings and applications,[8–12] and they also support a collection of unusual measurement modalities and capabilities. One important example is in quantitative evaluations of thermal transport properties of the skin, as the basis for insights into physical changes related to hydration, blood perfusion, and to various related pathologies.

Extensive recent work demonstrates the capabilities of soft, conformal sensors based on thin, thermal elements that simultaneously function as high-precision (30 mK) thermometers and precisely controlled thermal actuators for quantitative measurements of this kind. When laminated onto the surface of the skin, low-power thermal actuation (≈2 mW) results in localized heating to temperatures below the threshold for sensation ($\Delta T \approx 6$ K). Measurements of temperature at and/or near the point of actuation yield time-dependent data ($\Delta T(t)$) that can be analyzed using well-established algorithms[13,14] to determine the thermal conductivity (k) and thermal diffusivity (α). Measurements of temperature,[15] thermal conductivity,[16] and heat capacity (the product of the heat capacity at constant pressure and the density is equal to the ratio of k_{skin} to α_{skin})[17] made in this way can yield detailed information on blood flow,[8] skin hydration,[14] wound healing,[18] sunburn,[19] and cellulitis.[20] Such sensors can be configured to assess properties of near-surface regions of the skin or at depths of up to of several millimeters[20] across nearly any location on the body[21] even including the fingernail,[22] from which measurements of the underlying nailbed tissue are possible.

All reported embodiments of such sensors rely on wired connections for power supply and data collection, thereby limiting usability as in-home diagnostic systems, wearable monitors, or as research tools for large-scale dermatological studies. The following presents a set of concepts in materials science, mechanical engineering, and electronics design that, when combined in an optimized platform, yield a lightweight, epidermal wireless thermal sensor (eWTS) that can operate in a battery-free mode via a standard smartphone, or radio-frequency (RF) reader, where data and power transmission occur via resonant inductive coupling using near-field communication (NFC) protocols. Systematic experimental and theoretical studies establish key mechanical, electrical and thermal design considerations for 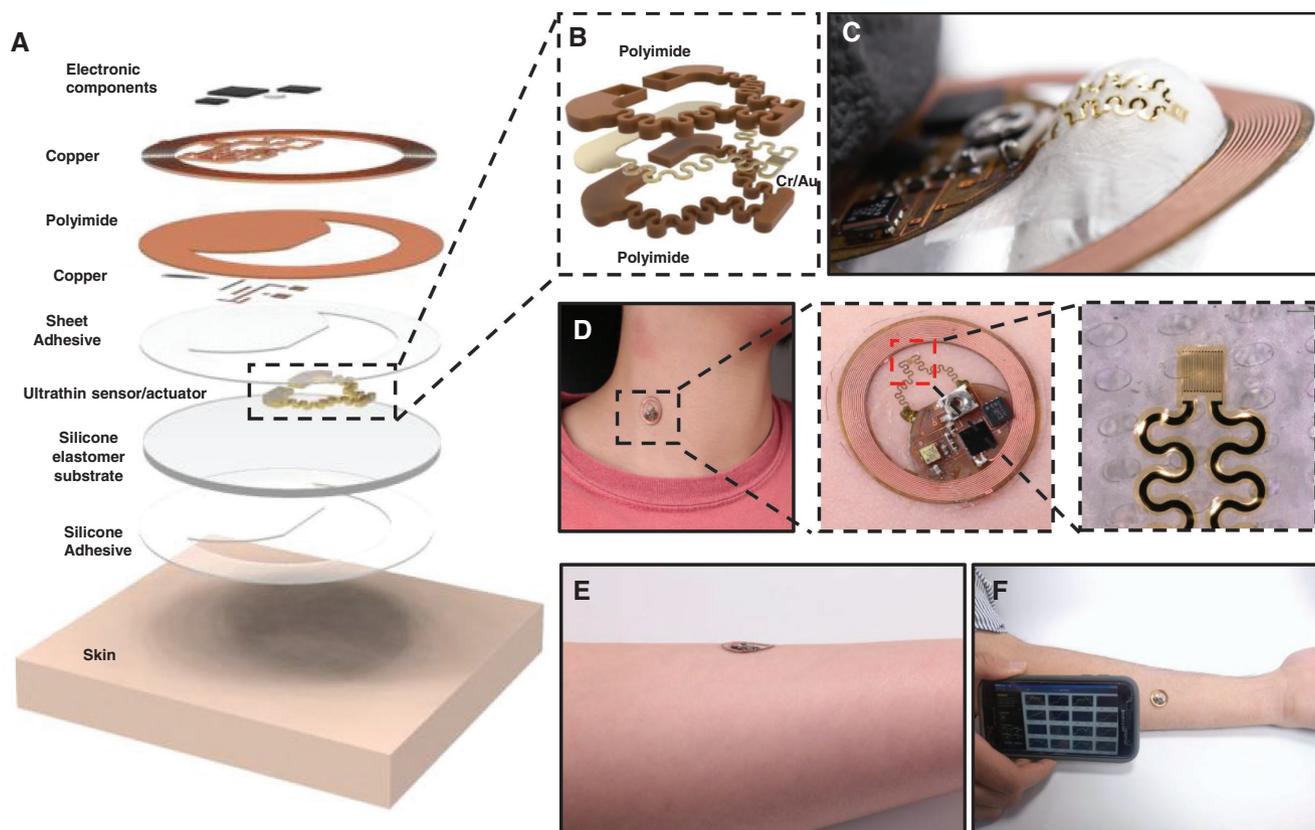stable device operation across a range of practical conditions, including continuous use over many days during natural activities. Experiments on human subjects with healthy skin and various skin pathologies illustrate capabilities in precision measurements of skin temperature and thermal conductivity, as well as their relationship to hydration and trauma. The results have potential applicability in areas ranging from skin care and cosmetics, to clinical health and athletic performance.

2. Results

2.1. Device Construction and Operation

The device platforms reported here rely on metallic elements in thin, stretchable platforms designed to efficiently transfer heat to underlying biological tissue and to monitor the resulting time-dependent variations in the temperature at the surface. The low thermal mass (<10 mJ cm^{-2} K^{-1}) of these sensors and their capacity to form intimate, conformal contacts to the skin are critical design considerations.[15] A schematic illustration of the eWTS appears in **Figure 1**A, highlighting these and other key features. The platform consists of two mechanically distinct components. The first incorporates an inductive coil for wireless power harvesting and a collection of electronic components for NFC-based data transmission and analog signal conditioning, all assembled on a flexible printed circuit board (flex-PCB; flexural rigidity, EI ≈ 3000 Pa m^3). This platform is compatible with commercial components and technologies, with sufficient thickness to offer robust mechanical properties for handling and manipulation. Mechanical characterization under different loading conditions appear in Figure S1 (Supporting Information). The second consists of a photolithographically defined pattern of Cr/Au (10/100 nm) encapsulated by a thin (3 µm) layer of polyimide (PI) on an elastomeric substrate (80 µm; EI ≈ 0.3 Pa m^3), as shown in Figure 1B. The Cr/Au trace forms a stretchable sensor/actuator with linear, low-hysteresis behavior based on a well-defined temperature coefficient of resistance (TCR), where the experimentally measured TCR (0.0027 Ω Ω^{-1} K^{-1}) correlates well with established values for thin gold films (0.0025–0.0034 Ω–Ω^{-1} K^{-1}),[23] as shown in Figure S2 (Supporting Information). The PI layers mechanically and electrically isolate this structure. The soft, stretchable mechanics are apparent in Figure 1C, where gentle pressure from a cotton-tipped applicator easily deforms and elastically stretches the device. In accordance with design rules in epidermal electronics,[24] the low flexural rigidity and the effective low modulus facilitate conformal contact with the skin. The heterogeneous combination of a flex-PCB platform and a soft, ultrathin sensor/actuator represents a design that unites the most advanced concepts in epidermal electronics with commercially mature manufacturing approaches.

An opening in the flex-PCB serves as the location for integrating the epidermal platform via an acrylate-based, pressure-sensitive label adhesive (JMS 1170). A low-temperature Indium-based solder establishes electrical contact between these two components. A thin (80 µm) medical grade adhesive allows for reversible bonding ($Q_{adhesion}$ = 880 N m^{-1}) of the flex-PCB to the skin. The sensor/actuator contacts the skin via the action of van der Waals forces ($Q_{adhesion} \approx 5$ N m^{-1}). The small

ADVANCED
SCIENCE NEWS
www.advancedsciencenews.com

NANO · MICRO
small
www.small-journal.com

Figure 1. Device design. A) Exploded view schematic illustration of an epidermal wireless thermal sensor (eWTS). B) Similar illustration of the ultrathin, soft, thermal sensing/actuating component. C) Optical image of a sensor held with a pair of tweezers. D) Optical image of a sensor mounted on the skin of the neck, illustrating constituent components. E) Side-view image of a device on the arm. F) Simulated readout with a smartphone using NFC protocols.

overall size ($D = 1.6$ cm), the low mass (200 mg), and the mechanical flexibility of the eWTS enable application on a range of body locations. An optical image of an eWTS on the neck of a human subject appears in Figure 1D, with enlarged views that highlight the key features outlined above. Application on the forearm allows for easy access with a smartphone, as shown in the optical images in Figure 1E,F.

Wired measurements using this type of sensor/actuator offer the ability to tune key experimental parameters and to reveal important design considerations in actuation power and measurement resolution, as in **Figure 2**. Here, mixtures of two commercially available silicone materials (Sylgard 184 and Sylgard 170, both from Dow Corning) with thermal conductivities that bound those of skin ($k_{syl\ 184} = 0.19$ W m^{-1} K^{-1}, $k_{syl\ 170} = 0.5$ W m^{-1} K^{-1}) form skin phantoms for in vitro characterization. Lamination of a wired sensor on a skin phantom prepared in this way, followed by simultaneous temperature sensing and low-power actuation, results in a characteristic transient rise in temperature ($\Delta T(t)$) whose behavior depends mainly on the thermal diffusivity ($\alpha_{phantom}$) of the underlying material for times shortly following actuation (<100 ms) and on the thermal conductivity ($k_{phantom}$) at longer times (>2 s),[19] for the designs reported here. Representative data collected from samples of pure Sylgard 184 and pure Sylgard 170 appear in Figure 2A, for two different actuation powers, P_{act}. Prior work shows that the thermal conductivity of the skin and correlates in linear

fashion to its hydration, across a range of physiologically relevant values.[14,19] As a result, the following discussion focuses on k. A simple, effective way of extracting k involves measurements of the change in local temperature at a known, fixed time interval after actuation ($\Delta T(t = t_{fixed})$). This quantity varies inversely with k, as shown in Figure 2A. Increasing P_{act} increases the change in temperature, resulting in larger absolute differences in ($\Delta T(t = t_{fixed})$) for materials with different k, as shown in Figure 2B, thereby facilitating precise measurements of k.

The results of Figure 2C highlight these effects through measurements of $\Delta T(t = 6$ s) on six skin phantoms with different weight fractions of Sylgard 170 in Sylgard 184 (0%, 20%. 40%, 60%, 80%, and 100%), where values of $k_{phantom}$ can be estimated by an effective medium model,[25] across six values of P_{act} (7.1, 5.0, 3.2, 1.8, 0.8, and 0.2 mW). Though the variation of $k_{phantom}$ with changing weight fractions of Sylgard 170 depends on a complex set of factors, including its morphology in the Sylgard 184 matrix, surface interactions, and the effects of percolation,[25] the relationship can be effectively quantified with a simple, second-order polynomial fit, as shown in Figure 2C. Averages and standard deviations follow from three successive measurements on each phantom for each P_{act}. The measurement precision decreases with decreasing P_{act}, as illustrated by the diminished correlation coefficients (R^2) for the fits, and the error bars increase due to increasing relative contributions to variability from ambient conditions such as convection and drift.
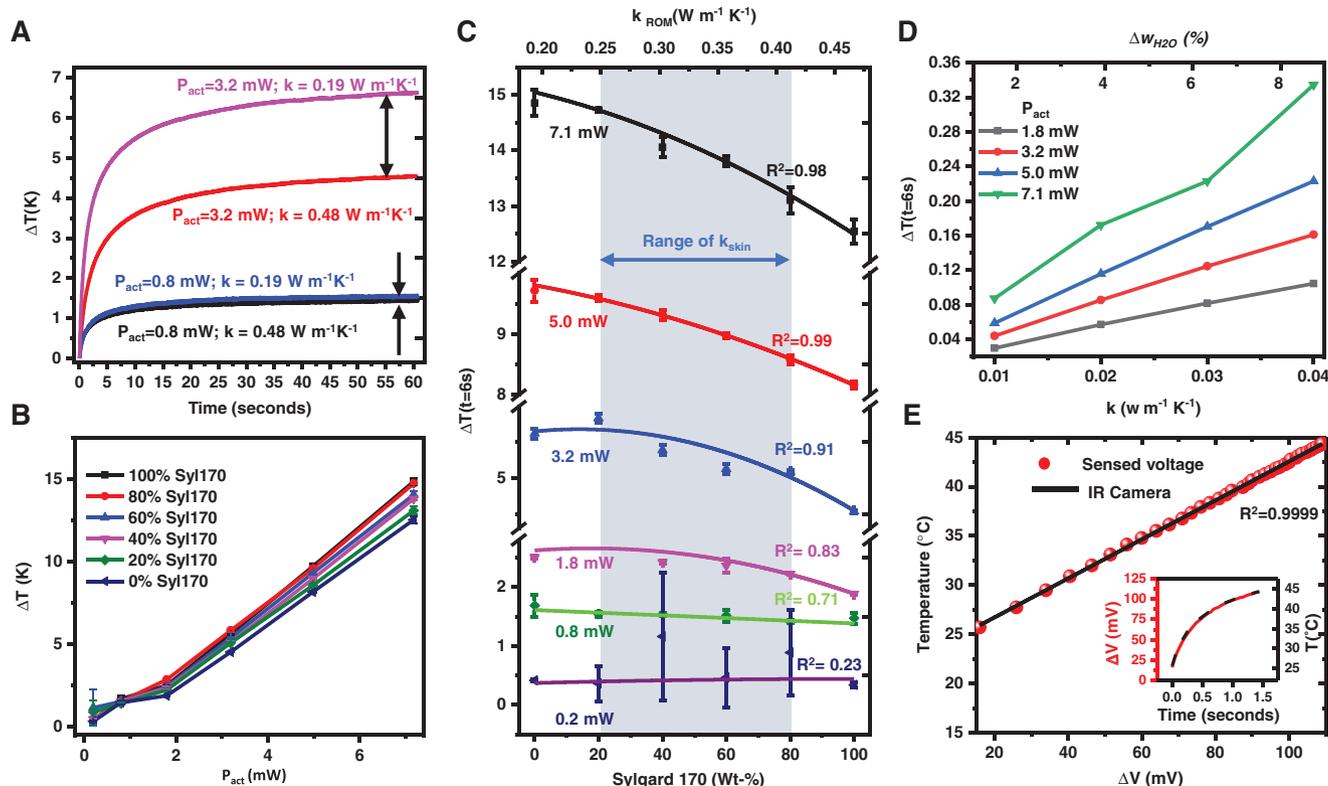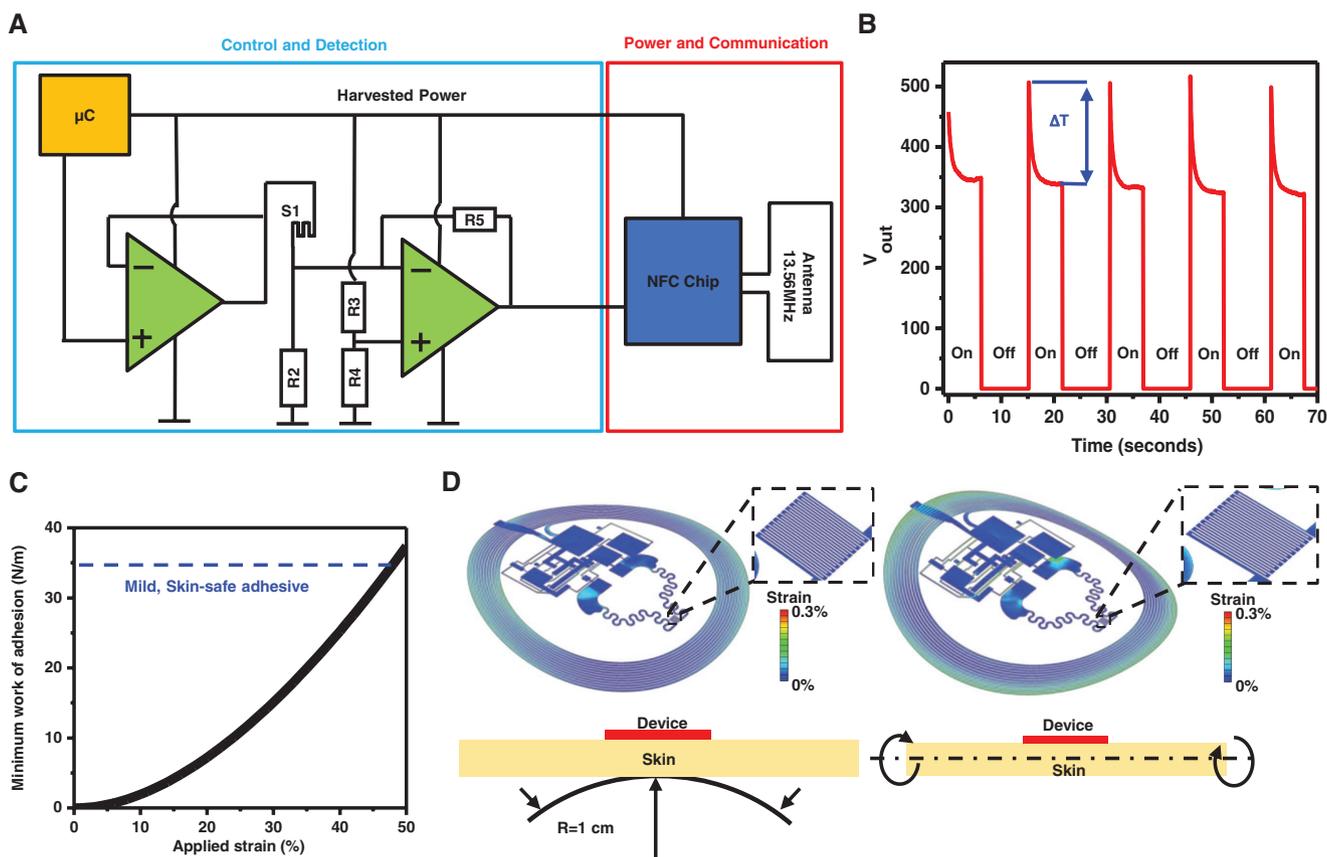
Figure 2. Studies of design requirements using a wired sensor. A) Transient temperature response at two different actuation powers (P_{act} = 3.2 and 0.8 mW), on two skin phantoms (Sylgard 184, red and black curves and Sylgard 170 blue and pink and blue curves) representing the extremes of skin (k_{syl170} = 0.50 W m^{-1} K^{-1}, k_{syl184} = 0.19 W m^{-1} K^{-1}). The results highlight the coupling between actuation power and resolution. B) Temperature rise 6 s after actuation for a range of P_{act} for mixtures of Sylgard 170 and Sylgard 184 with thermal conductivities that span the range commonly encountered in human skin. C) $\Delta T(t = 6$ s) as a function of ratio between Sylgard 170 and Sylgard 184, with second-order polynomial fits and associated R^2 values for a range of actuation powers. D) Computed curves showing changes in measured values of $\Delta T(t = 6$ s) as a function of changes in k, with changes in hydration as weight percentage in skin from effective medium computations. E) Conversion of wirelessly measured voltage to temperature via a calibration with an IR camera showing experimentally achieved resolution and goodness of fit, with raw data (inset).

The correlations shown in Figure 2C can be used to convert changes in k (Δk), a derived quantity, to changes in $\Delta T(t = 6$ s)), a directly measurable quantity, as shown in Figure 2D for different values of P_{act}. Measurements of changes in skin hydration (water content, by wt%, $\Delta w_{H2O,skin}$) form an important application of the eWTS platform, and values of Δk_{skin} can be translated to relative measurements of $\Delta w_{H2O,skin}$ using effective medium models, details of which appear in Figure S3 and Note S2 in the Supporting Information. The results of this conversion are in Figure 2D. The resolution in $\Delta T(t)$ realized with the analog front-end design implemented here (shown in Figures S4 and S5 and discussed subsequently in the Supporting Information) is ≈80 mK, as confirmed by quantitative comparison to IR imaging. The implication is a measurement precision in Δk of 0.02 W m^{-1} K^{-1} for P_{act} = 2 mW, which corresponds to a precision in Δw_{H2O} of <5%, in agreement with previous reports.[15] Additional validation studies appear in Figure S4 (Supporting Information).

The electronics rely on energy harvesting and communication through a 13.56 MHz antenna with a high Q factor (Figure S5, Supporting Information). The harvested power operates the complete circuit, including a microcontroller (ATTiny10) that enables precise timing and control over the thermal actuation of the eWTS and an analog driver and amplifier that allow high resolution, wireless measurements of $\Delta T(t)$. A schematic of the overall circuit appears in **Figure 3**A. The sensing section of the circuit is built around the resistive, thin-film metallic element ($S1$ ≈ 650 Ω), as the sensor/actuator, located at one arm of a balanced Wheatstone bridge ($R2$, $R3$, $R4$). Changes in temperature cause changes in resistance in $S1$ that are governed by the TCR of the thin metallic film its constructed from. For example, a local temperature increase of 5 K results in a resistance increase in $S1$ of ≈10 Ω, resulting in differential voltage changes (≈500 µV) with respect to the reference arm of the bridge. This differential voltage is amplified by an operational amplifier whose closed-loop gain is set by a feedback resistor ($R5$). To induce thermal actuation, the $S1$ timing is controlled by the microcontroller whose signal is buffered by an operational amplifier in a voltage-follower configuration that is on the same die (ADA 4505-2, Analog Devices Inc.) as the operational amplifier to ensure robust operation in an RF field. The value of $R2$ can be tuned manually via a miniaturized potentiometer (TC42X-2-202E, Bourns Inc.) to control the power dissipated in the sensing arm of the Wheatstone bridge. The amplified signal feeds into the analog-digital converter (ADC) of a bare-die NFC chip (AMS SL13A, AMS Inc.) that features a 10 bit ADC with a full range of 300 mV (300–600 mV). The resulting temperature resolution is ≈80 mK, consistent

ADVANCED
SCIENCE NEWS
www.advancedsciencenews.com

NANO · MICRO
small
www.small-journal.com

Figure 3. Electrical designs and results of thermal characterization. A) Schematic illustration of the circuit design, showing components responsible for sensing, control, and wireless power harvesting and data transmission. B) Wirelessly recorded sensor output, during sequential actuation at 0.067 Hz frequency and 33% duty cycle, showing measured changes in voltage due to thermal actuation. C) Computed minimum work of adhesion between an eWTS and the skin as a function of uniaxial strain, showing strains at which skin yields and tears, respectively. D) Strain distribution in an eWTS during bending (left) and twisting (right) showing nearly 0% strain at the receiver coil and the resistive sensing/actuating element.

with measurements described previously. Raw data recorded from the sensor (V_{out}) by an NFC reader appear in Figure 3B, illustrating periods of actuation (On) and inactivity (Off), and transient changes in V_{out} induced by actuation ($\Delta T(t)$). Further details of the circuit are in the LTSpice simulations of Figure S6 (Supporting Information).

Strains encountered in practical use cases can, potentially, delaminate the sensor from the skin, and/or affect resistive temperature measurements. As such, robust mechanical designs are essential to reliable operation. Even slight, partial delamination can significantly alter the measurement results because air has a thermal conductivity that is an order of magnitude lower than that of the skin and other soft tissues.[26] 3D finite element analysis (3D-FEA) indicates that the minimum work of adhesion required to maintain conformal contact between the skin and the eWTS for large, applied uniaxial strains (15%) that represent the practical limits for skin is ≈5 N m^{-1}. This requirement can be satisfied with skin-safe silicone or acrylate-based adhesives (work of adhesion > 50 N m^{-1}[27]) as shown in Figure 3C. The required work of adhesion is low because the energy release rate, which is responsible for delamination, decreases with the device size[28] and the device diameter is only 16 mm.

The corresponding deformations of the device under these conditions and others such as twisting and bending, as shown

in the 3D-FEA results of Figure 3D, result in peak strains of <0.1% in the copper antenna coil and in other key regions. Additionally, placement of the sensor/actuator near the neutral mechanical plane of the PI–metal–PI assembly (thicknesses of 3 µm, 110 nm, and 3 µm) results in similarly small strains (<0.1%), as shown in the inset images in Figure 3D. To summarize, the mechanical designs introduced here enable 1) strong, reversible, conformal contact between the skin and the sensor/actuator, 2) robust operation with commercial surface mounted (SM) analog and NFC electronic components, and 3) strain isolation of the sensor/actuator, the NFC antenna, and bare-die components. The construction leverages technologies in microfabrication, transfer printing, and laser structuring that are inherently scalable and aligned with low-cost manufacturing.

2.2. Thermal Characterization of Soft Materials and Fluids

Extensive comparisons to wireless data, IR imaging, and FEA models validate the measurement capabilities of the eWTS platform. **Figure 4**A shows IR thermographs of the sensor/actuator during operation in air (left) and on human skin (right). During actuation (i.e., the "On" period), 2 mW of thermal
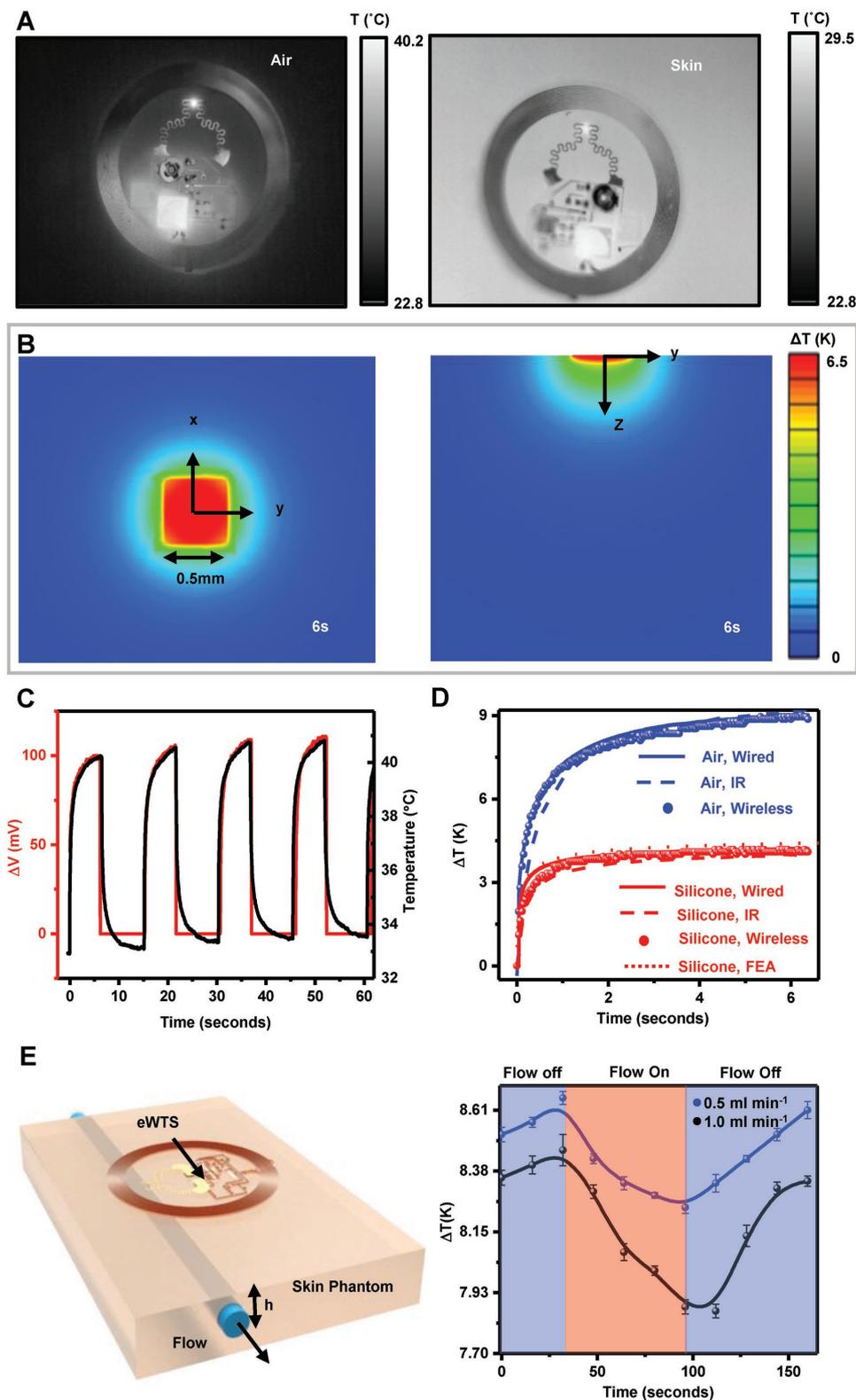
Figure 4. Wireless measurements on biological phantom systems. A) IR thermographs of eWTS in air (left) and on a subject's skin (right). B) Temperature distributions computed by 3D-FEA (top view (left) and side view (right)) 6 s after actuation at 2 mW. C) Wirelessly measured voltage during actuation, with IR thermography results acquired simultaneously. D) IR imaging, data acquired with a wired system, data acquired using an eWTS and 3D-FEA model for $\Delta T(t)$ for the case of air and a silicone skin phantom ($k_{phantom} = 0.5$ W m^{-1} K^{-1}). E) Schematic illustration (left) and measured transient temperature rise 6 s after actuation (right) on a benchtop flow system designed to mimic near-surface blood vessels and catheters.

ADVANCED
SCIENCE NEWS
www.advancedsciencenews.com

NANO · MICRO
small
www.small-journal.com

power results in localized heating across a region with spatial extent defined by the properties of the sensor/actuator and the surrounding materials. The low thermal conductivity of air ($\approx$0.02 W m^{-1} K^{-1}) relative to skin ($\approx$0.32 W m^{-1} K$^{-1[26]}$) results in a higher local temperature rise in air than in skin. 3D-FEA simulations of heat flow through skin reveal that after actuation for 6 s, the characteristic depth of penetration of the heat is $\approx$1 mm (within the epidermis) and the $\Delta T(t = 6$ s)) at the surface is $\approx$6.5 K. Note also that the NFC chip itself is a source of localized heating, as seen in Figure 4A. The overall layout of the device ensures, however, that the chip is sufficiently far from the sensor/actuator that its heating has little effect on the measurement, as shown in Figure S7 (Supporting Information).

Operation of the eWTS at 0.05 Hz and 33% duty cycle, results in data shown in Figure 4C. Comparing the measured voltage (red curve) with data from IR thermographs (black curve) yields a linear calibration that converts voltage to temperature. In this way, both the temperature rise ($\Delta T(t)$) and the starting temperature ($T(t = 0)$) associated with each cycle of actuation yield data on thermal transport and baseline temperature, respectively. Drifts in the starting temperature ($T(t = 0)$) do not affect the temperature rise, as shown in Figure S8 (Supporting Information). Wireless measurements match those obtained with previously described wired systems, as shown in Figure 4E with IR imaging and with FEA simulations for a silicone skin phantom (Sylgard 170, $k = 0.50$ W m^{-1} K^{-1}). As expected, the $\Delta T(t)$ measured on air and Sylgard 170 shows dramatic differences, where the data from Sylgard 170 exhibit a lower slope $\left(\dfrac{\mathrm{d}T(t)}{\mathrm{d}t}\right)$ at short time scales ($t < 1$ s) and a lower saturation temperature ($\approx$4 K, at $t = 6$ s) than those of air (>8 K), consistent with the large differences in thermal transport properties of these two materials.

In addition to thermal conductivity, measurements of this type can also quantify the convective effects of fluid flows near the surface of the sample under test, of relevance for quantifying rates of flow of biofluids in or under the epidermis. Studies performed using a slab of silicone with a catheter tube located at a depth of 1 mm, as shown in Figure 4E (top), illustrate the capabilities. The results in Figure 3D (bottom) correspond to operation of the eWTS at 0.05 Hz and 33% duty cycle for flow rates comparable to those associated with blood flow through macrovessels and near-surface subdermal catheters ($Q_{\text{flow}} = 0.5$ and 1.0 mL min^{-1}).[29] These data can be converted into flow rates using numerical models or calibration procedures.[30] A representative calibration appears in Figure S9 (Supporting Information).

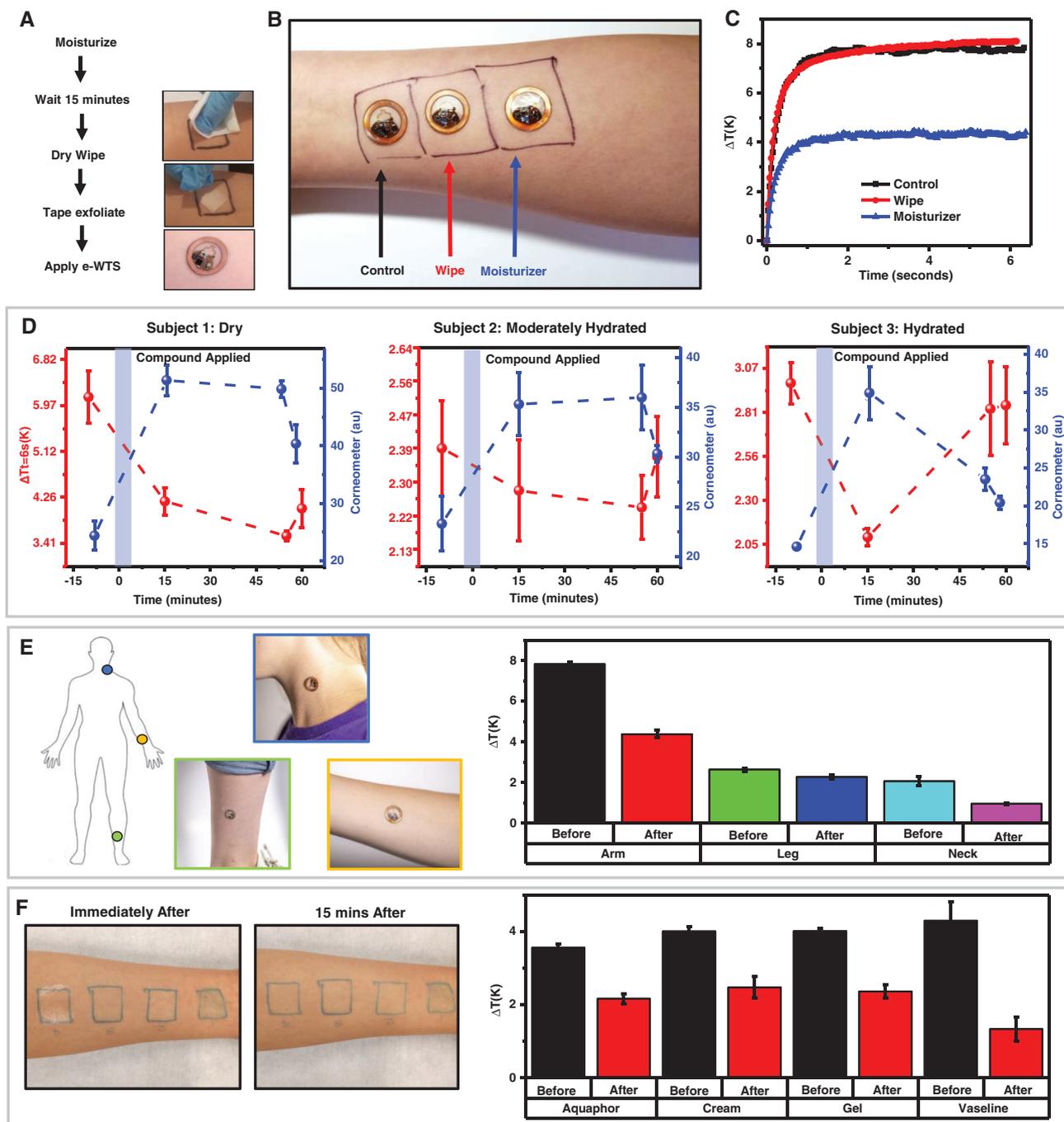## 2.3. Human Subject Studies of Skin Hydration

The human epidermis is a complex structure that consists of cornified outer layers and viable inner layers. The outer layers largely consist of squamified cells (corneocytes) and an interlayer lipid matrix, which, taken together, form a "brick and mortar" structure that prevents transepidermal water loss and absorption of airborne pollutants and pathogens via diffusion.[31] Free water in these layers serves a critical structural role in maintaining the parallel, lamellar structure of the lipid

matrix, by forming hydrogen bonds to the polar head groups of the lipids. Typical moisture levels in the outer layers of the epidermis, such as the stratum corneum (SC) and stratum granulosum, are $\approx$20%. Levels that fall below $\approx$10%[31] result in poor barrier properties and the appearance of dry, flaky skin. Consequently, measurements of skin hydration are important in fields as diverse as dermatology, toxicology, and sports medicine.

The validation studies described above support the use of the eWTS platform for characterization of hydration levels in skin.[32] The existing commercial gold standard, an impedance-based measurement probe (Moisturemeter, Delfin Systems GmbH), provides a benchmark for comparison.[6] The series of images in **Figure 5**A highlight a procedure for studies that include an incubation time for the moisturizer to fully absorb into the skin and a process of eliminating any residual material by application and removal of a piece of tape (Scotch brand, 3M Inc.). Measurements include three adjacent locations on the right volar arm of a healthy subject (female, age 23) using three separate eWTS devices. One is treated with an alcohol wipe, another with a commercially available cream-based moisturizer (Nivea Inc.), and the third with a dry wipe. A single system of control and readout electronics allows successive wireless measurements from each sensor. An image of the experimental setup is in Figure 5B. The chosen moisturizer consists primarily of a hydrophobic humectant (glycerine), where a topically applied thin film of 5 mg cm^{-2} acts a barrier to escaping water from deeper, epidermal layers. The large gradient in water concentration that exists across the thickness of the epidermis (70% water by weight in the viable, deeper layers of the epidermis to 20% in a healthy stratum corneum[33]) ensures strong diffusive transport of free epidermal water to the superficial skin layers, where it is trapped by the humectant.

Increased water content in the dry, outer layers affects thermal transport in two ways. First, the primary structural constituent of dry skin is type I collagen,[34] with $k_{\text{collagen}} = 0.15$ W m^{-1} K^{-1}. Because water has a thermal conductivity of $k_{\text{water}} = 0.61$ W m^{-1} K^{-1} (at 300 K), an increased filling fraction of water in the collagen matrix will increase the thermal conductivity of the skin, k_{skin} as predicted by simple effective medium models, such as those shown in Figure S3 (Supporting Information).[14] Second, physical swelling and extension of the polymers of the skin matrix that follows from increases in free water content result in an increased phonon mean free path.[25,35] Taken together, these effects enhance thermal transport through skin, consistent with values of $\Delta T(t)$ observed before and after the application of the moisturizer in Figure 5C. The case of the alcohol wipe shows no discernible effect.

Results of measurements on three healthy subjects (Figure 5D) reveal high levels of variability in the efficacy of topical moisturizers due to the complexity in the underlying mechanisms and the inhomogeneity of skin types. Application on the visibly dry, flaking skin on the volar forearm of subject 1 (male, age 26) leads to a large change in hydration, as captured by both the moisturemeter and the eWTS ($\Delta T(t = 6$ s)). For skin with healthy appearance, the effect of the topical compound is smaller with subject 2 (male, age 23) than with subject 3 (female, age 24). In all three cases, measurements show a

ADVANCED
SCIENCE NEWS
www.advancedsciencenews.com

NANO · MICRO
small
www.small-journal.com

Figure 5. Wireless measurements of skin hydration on human subjects. A) Schematic illustration and optical images of a protocol for experiments using topical compounds. B) Optical image of multiple sensors on the arm of a subject. Measurements involve sequential read out using a single device, each on locations with different treatments. C) Data recorded sequentially from the three locations shown in panel (B). D) Time series measurements with an eWTS and a moisturemeter on three subjects with different hydration levels before and after the application of a topical moisturizing compound. E) Schematic illustration of body locations for application of a topical moisturizer (Vaseline; left) and measured transient temperature rise before and after application of moisturizer. F) Optical image of a subject's arm immediately after application of four different topical compounds, Aquaphor, Cream, Gel, and Vaseline (left) and 15 min later, after dry-wiping and tape exfoliation (right). Transient temperature response before and 15 min after application of each of these compounds. The "after" measurements are performed after dry-wiping and tape-exfoliation. In all cases, error bars correspond to standard deviations computed across three measurements.

decrease in the hydrating effects with time, where the properties of the skin return to 70%, 96%, and 100% of their initial values 60 min after application, consistent with previous reports, likely due to wrinkle-induced defects in the cream. The continuous natural exfoliation of the stratum corneum also plays a role at longer time scales, allowing for diffusive water loss.
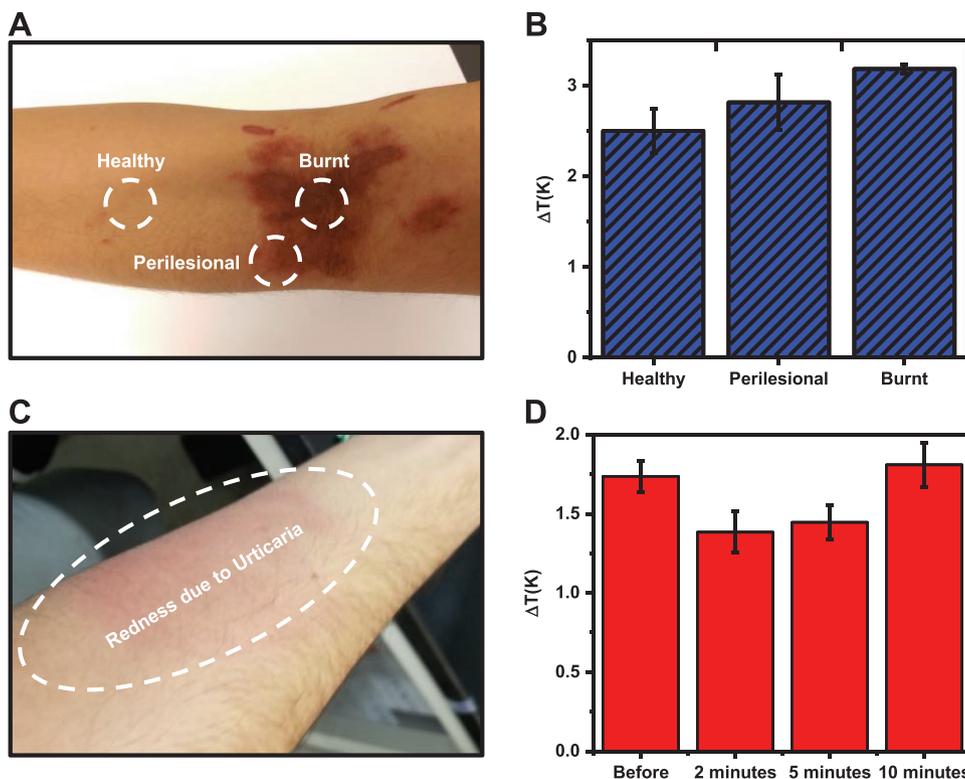
Figure 6. Human subject studies of changes in the thermal properties of skin due to trauma. A) Optical image of a subject's arm, collected 2 days after suffering burns, showing burnt, healthy, and perilesional locations. B) Measured temperature increase 6 s after actuation at each of these three locations. C) Optical image of a subject's arm 2 min after dermatographic urticaria, showing inflammation and redness. D) Measured temperature increase 6 s after actuation before, and 2, 5, and 10 min after urticaria.

These platforms can be easily mounted on different body locations, as illustrated by studies on the arm, neck, and leg shown in Figure 5E (left). Measurements before and 15 min after the application of moisturizer on a healthy subject (female, age 24) indicate that the strongest effects occur on the arm, followed by the neck, and then the leg, as shown in Figure 5E (right). Evaluations of different types of moisturizers highlight the dependence on the chemistry of these materials. Optical images immediately after, and 15 min after application of petrolatum, aloe gel, lotion, and cream appear in Figure 5F. In general, moisturizers rely either on the occlusive action of humectants (e.g., Vaseline, a type of petrolatum) to reduce rates of transepidermal water loss, the absorptive effects of emollients (e.g., gel) to trap ambient moisture, or some combination of these. Measurements shown in Figure 5F reveal that pure petrolatum (Vaseline) induces the most pronounced changes in hydration, due to its lipid-rich structure, consistent with previous reports.[31,36] Different types of moisturizing treatments result in different hydration profiles across the thickness of the epidermis,[37] suitable for probing with thermal techniques like those described here.[7]

2.4. Human Subject Studies of Changes in Thermal Transport of the Skin Due to Trauma

Blood flow through near surface vessels can also affect thermal transport through near-surface skin layers, particularly, the upper dermis and lower epidermis. This type of flow is not directional, as in a macrovessel such as a vein or artery, but rather represents isotropic thermal transport that can be modeled as a modification of the heat diffusion equation (HDE) that incorporates volumetric perfusion.[38–42] Here, an increase in perfusion results in an effective increase in k_{skin}. By contrast, trauma, such as a class II burn injury, leads to ischemia and ultimately necrosis in dermal layers, causing a significant reduction in viable, perfused tissue, and therefore a reduction in k_{skin}.[43] Optical images of the right volar forearm of a burn victim (female, age 23) are in **Figure 6**A, showing burnt, perilesional skin and healthy skin. The reduced rates of thermal transport in burnt skin, relative to healthy and perilesional skin, are apparent in measurements performed 2 days after the burn, on each of the three skin types highlighted above Figure 6B.

In contrast to burn-induced reductions in near-surface perfusion, other types of skin trauma such as slap-induced dermatographic urticaria results in inflammation and hyperemia, apparent as redness on the volar forearm of an otherwise healthy subject (male, age 26) in Figure 6C. Hyperemia results in increased rates of thermal transport due to the increased volume of blood perfusing the same control volume of tissue.[40] Typical symptoms of inflammation due to urticaria last ≈10 min,[30] consistent with the data of Figure 6D that suggest initial increases in thermal conductivity that gradually return to their baseline values.

ADVANCED
SCIENCE NEWS
www.advancedsciencenews.com

NANO · MICRO
small
www.small-journal.com
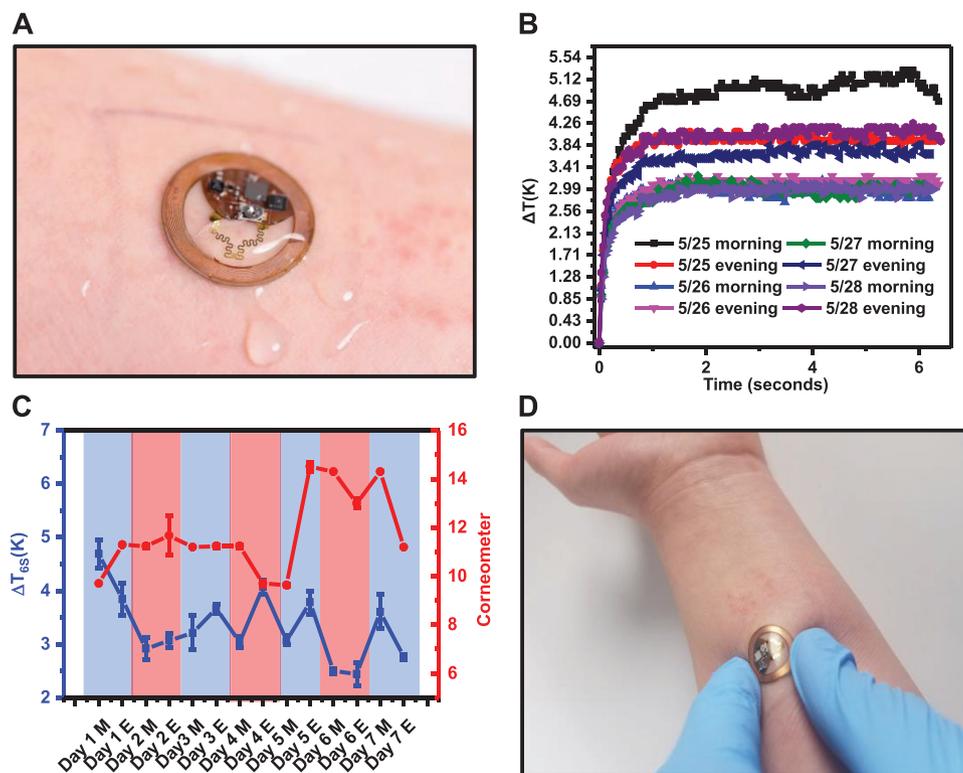
Figure 7. Human subject studies of changes in the thermal properties of skin due to trauma. A) Optical image of a wet eWTS, simulating shower conditions. Water does not affect the electronics. B) $\Delta T(t = 6\text{ s})$ measured over 7 days, showing stable operation. C) Measured temperature rise measured 6 s after actuation, collected twice per day over 7 days, with comparison to measurements using a moisturemeter at adjacent skin locations. D) Optical image of the volar aspect of a subject's left forearm with an eWTS after 7 days of continuous wear.

2.5. Continuous, Stable Operation in a Range of Conditions

The miniaturized, rugged construction, the flexible mechanics, the lightweight, battery-free operation, and the waterproof designs of the eWTS platform allow continuous wear and monitoring over many days. As a demonstration, a subject (female, age 24) wore the eWTS for 1 week, without disruption to routine activities such as exercise, showering, and sleeping. Here, a thin, breathable layer of medical tape (Tegaderm, 3M Inc.) covered the device (further images with covered eWTS are in Figure S10 in the Supporting Information). The NFC protocols are insensitive to ambient water content,[44] thereby allowing for stable operation even during complete immersion in water, as illustrated in **Figure 7**A, although such conditions strongly influence the thermal characterization results.

Raw data ($\Delta T(t)$) from measurements performed twice a day (at 10:00 am and 5:00 pm) throughout the testing period illustrate the reliability and stability of the measurement, as summarized in Figure 7B. Measured values of $\Delta T(t = 6\text{ s})$ along with data collected using the moisturemeter applied at adjacent locations of the skin validate the measurements are shown in Figure 7C. As expected, the two quantities vary inversely with each other, with increased hydration resulting in increased values of k_{skin}. In the absence of external moisturizing compounds or treatments, variations in hydration are likely influenced by fluctuations in ambient temperature and humidity,[1,31,45] with further data in Figure S11 (Supporting Information). The eWTS forms a nonirritating, comfortable interface for the user, as supported by an optical image recorded after 1 week of continuous use (Figure 7D) that reveals no signs of inflammation or irritation.

3. Discussion

3.1. Error, Noise, and Uncertainty

The analog circuit designs reported here support measurement precision of ≈ 20 mK, but are constrained by software limitations, resulting in a measurement precision of ≈ 80 mK, capable of resolving the thermal conductivity to 0.02 W m^{-1} K^{-1}, as discussed above. The effects of decreased measurement precision in temperature are apparent in Figure S12A,B (Supporting Information). For a temperature resolution that is worse than 300 mK, the measurements can only distinguish skin phantom materials with differences in thermal conductivity that are larger than ≈ 0.05 W m^{-1} K^{-1}. Effects of the surface texture of the skin and convective transport due to ambient air flows appear in Figure S12C (Supporting Information). The latter studies use flat silicone samples and the former use textured silicones created by casting against a relief pattern created by a fingerprint. Measurements show differences of <2% in $\Delta T(t = 6\text{ s})$ with error bars from standard deviations across three measurements that exhibit an increase of $\approx 5\%$ from the untextured case. Studies of the effects of convection involve measurements with the device in an enclosure to prevent air

currents. Comparisons to measurements made without the enclosure show values of $\Delta T(t = 6\ s)$ that are <5% higher than those of the uncovered case, due to the effects of convective cooling. These two measurement conditions yield nearly identical (<1%) standard deviations, likely due to the short (6 s) measurement times.

An additional consideration in measurement performance is a timing uncertainty of 40 ms that is inherent to the ADC sampling rate and communication protocol of the NFC Chip (ISO 15693). Multiple measurements, typically five in succession with the highest and lowest values discarded and the remaining three values averaged, can minimize the effects of such uncertainties. The error bars suggest 5–10% measurement uncertainty. Finally, we note that the precision of our system is limited by the wireless software readout to 1 mV, and, as such, the contributions of ambient and RF noise play a minimal role relative to code transition noise as seen in Figure S12D (Supporting Information).

3.2. Implications for Clinical Monitoring

The results presented here establish a set of concepts in electrical, mechanical, and materials design as routes to lightweight, wearable sensors for multimodal thermal characterization with precision comparable or superior than that of the clinical gold standard. The versatility and robustness of the sensing platform allow for precise measurements of temperature, skin hydration, and changes in vascular perfusion associated with trauma and wound healing, suggesting broad utility in clinical monitoring. The rugged, lightweight, battery-free design allows for continuous use over periods spanning a week, with power and data transmission via NFC protocols that are available on most smartphones and stationary radio-frequency identification (RFID) readers. The sensor design suggests pathways for low-cost scaling and manufacture to meet the demands of large study populations, with ultimately utility in clinical and at home monitoring performed by nonspecialist users.

4. Experimental Section

Fabrication of the Epidermal Sensor: Fabrication began with spin casting a sacrificial layer of (poly)methyl methacrylate (PMMA 495, A5, Microchem, 1.2 µm) on an undoped 4″ silicon wafer followed by spin casting and curing a layer of polyimide (PI 2545 HD Microsystems, 3 µm). Electron beam evaporation and photolithographic patterning defined a bilayer of Cr/Au (10/100 nm) into a geometry suitable for use as a thermal sensor/actuator. A second layer of PI (3 µm), spin cast and cured, completely encapsulated the sensor/actuator and electrical interconnects. Photolithography followed by O_2 plasma reactive ion etching (RIE) patterned the PI into the desired geometry and created openings for external electrical connections. Immersion in warm acetone removed the PMMA and allowed retrieval of the entire structure onto a cellulose-based, water-soluble tape (Aquasol Inc.). Depositing a layer of SiO_2 onto the back side facilitated bonding to a thin layer of (poly)-dimethyl siloxane (PDMS) (Sylgard 184, Dow Corning, 100 µm) on a PMMA-coated glass slide (75 mm × 50 mm). Exposing the PDMS to ozone in a UV–O cleaner for 5 min resulted in bonding to the SiO_2 on the device upon physical contact via condensation reactions of —OH groups at the surface. Warm water dissolved the water-soluble tape, leaving behind the device on the PDMS.

Fabrication of the Flex-PCB and Integration with the Epidermal Sensor: Fabrication began with laser structuring a commercially available high-density, electrodeposited trilayer film of copper/PI/copper (18 µm/75 µm/18 µm, Pyralux, DuPont Inc.), followed by successive cleaning in baths of flux (Worthington Inc.) isopropanol and deionized water. Key active and passive components (NFC Chip, microcontroller, operational-amplifier, matching capacitors, bridge resistors, and tuning resistors) were assembled via reflow soldering with low-temperature solder (Indium Corporation). A commercially available acrylate-based, pressure-sensitive adhesive (JMS, 1170) mechanically bonded the flex-PCB to the soft sensor, and low-temperature reflow soldering established electrical connections.

Simulation of the Circuit: The device elements associated with the analog front end were simulated using a circuit model on a freely available software package (LTSpice). Varying critical parameters allowed for facile tuning of the circuit, that allowed for efficient, high-throughput fabrication. Further details of the model are shown in Figure S5 (Supporting Information).

Thermal Characterization: Experiments involved mounting eWTS devices onto substrates with thicknesses greater than the penetration depth of the thermal field (>5 mm) and recording data from five successive actuation cycles. Discarding the highest and lowest values eliminated the outliers, and the remaining three measurements yielded the average value and standard deviation. Simultaneously collected thermographs from an IR camera ((FLIR A6255sc, FLIR Systems Inc.) validated the measurements.

Thermal and Mechanical FEA Models: The commercial software ABAQUS (ABAQUS Analysis User's Manual 2010, V6.10) determined the thermal conductivities of the skin in different conditions by fitting experimental results. Hexadedron elements (DC3D8) modeled the thermal sensor with a minimal mesh size of 1/4 of the wire width (2.5 µm) of the thermal sensor. FEA also provided mechanical insights. The device was mounted on skin (50 × 40 × 2 mm³) and subjected to bending and twisting. For bending, the displacement field applied to the bottom surface of the skin corresponded to a bending radius of $R = 1$ cm (Figure 3D). For twisting, the two ends of the skin were subjected to 180° relative rotation (Figure 3D). The PDMS substrate, skin, and adhesive layer were modeled by hexahedron elements (C3D8R), while the thin Cu, Au, and PI films were modeled by composite shell elements (S4R). The number of elements in the model was ≈10^7, and minimal mesh size was also 1/4 of the wire width (2.5 µm) of the thermal sensor in the mechanical simulation. The mesh convergence of the simulation was guaranteed for all cases. The elastic modulus and Poisson's ratio used in the simulations were: 1 MPa and 0.5 for the PDMS substrate; 0.13 MPa and 0.5 for the skin; 0.06 MPa and 0.5 for the adhesive; 119 GPa and 0.34 for Cu; 79 GPa and 0.4 for Au; and 2.5 GPa and 0.34 for PI.

Human Subject Studies: Each subject gave full, informed, signed consent before participating in on-body experiments. The data acquisition for all the trials reported below followed the same procedure, and was as follows. Mounting the eWTS on relevant skin locations and recording data from five successive actuation cycles yielded raw data. Discarding the highest and lowest values of each of these measurements and computing averages and standard deviations for ($\Delta T(t = 6\ s)$) from the resulting curves produced experimental data points and error bars, respectively.

Studies of Skin Hydration: The trial began by identifying locations on the volar forearms of consenting volunteers devoid of near-surface macrovessels. After 15 min following initial application, exfoliating the surface by applying and removing a piece of tape and then cleaning with a fresh, dry wipe removed residual moisture. The same procedures yielded "after data points. Evaluations using a moisturemeter (Delfin Systems gmbh) simultaneously with eWTS measurements provided some comparison data. An acrylate fiber-based ultrathin (80 µm) medical grade adhesive (3M Inc.) laser cut into the shape of the device, facilitated mounting on the skin.

Studies of Skin Burns: The trial began by identifying locations of severe burns on the right volar forearm of a volunteer (female, age 24), followed by demarcation into burnt, perilesional, and healthy locations,

**ADVANCED
SCIENCE NEWS**

www.advancedsciencenews.com

**NANO · MICRO
small**

www.small-journal.com

and the measurement procedure listed above. Simple, untreated Sylgard 184 (Dow Corning), relying solely on van der Waals interaction and without the use of any adhesives formed the interface between the sensor and the burnt skin.

Studies of Slap-Induced Dermatographic Urticaria: The trial began by identifying a region of the volar forearm of an informed, consenting volunteer (male, age 26) who was devoid of prominent near-surface blood vessels. Administering a single slap with three fingers resulted in an immediately apparent hyperemia and redness. Measurements with an eWTS followed the procedures listed above, at 120, 300, and 600 s after the redness became apparent.

Long-Term Monitoring: Mounting an eWTS on the volar forearm of a subject using the procedures listed above, and then covering the sensor with a single layer of conformal, breathable medical dressing (Tegaderm, 3M Inc.) served as the starting point for the studies. The volunteer performed normal routine activities such as sleeping, showering, and exercising over 7 successive days. Measurements were performed indoors each day, at 10:00 am and 5:00 pm. Three successive measurements with the moisturemeter, performed at the same time as those with the eWTS, yielded data for comparison. Weather logs for Evanston, IL, USA, for the dates and times of the study (weather.com Inc.) yielded ambient temperature and humidity data.

Supporting Information

Supporting Information is available from the Wiley Online Library or from the author.

Conflict of Interest

The authors declare no conflict of interest.

[1] I. H. Blank, J. Moloney, A. G. Emslie, I. Simon, C. Apt, *J. Invest. Dermatol.* **1984**, *82*, 188.

[2] D. Brebner, D. M. Kerslake, J. Waddell, *J. Physiol.* **1956**, *132*, 225.

[3] R. O. Potts, M. L. Francoeur, *J. Invest. Dermatol.* **1991**, *96*, 495.

[4] R. J. Scheuplein, *J. Invest. Dermatol.* **1967**, *48*, 79.

[5] A. Agache, P. Humbert, *Measuring the Skin*, Springer Science & Business Media, Berlin **2004**.

[6] E. Alanen, J. Nuutinen, K. Nicklén, T. Lahtinen, J. Mönkkönen, *Skin Res. Technol.* **2004**, *10*, 32.

[7] P. Girard, A. Beraud, A. Sirvent, *Skin Res. Technol.* **2000**, *6*, 205.

[8] R. C. Webb, Y. Ma, S. Krishnan, Y. Li, S. Yoon, X. Guo, X. Feng, Y. Shi, M. Seidel, N. M. Cho, J. Kurniawan, J. Ahad, N. Sheth, J. Kim, J. G. Taylor VI, T. Darlington, K. Chang, W. Huang, J. Ayers, A. Gruebele, R. M. Pielak, M. J. Slepian, Y. Huang, A. M. Gorbach, J. A. Rogers, *Sci. Adv.* **2015**, *1*, e1500701.

[9] J. Kim, A. Banks, H. Cheng, Z. Xie, S. Xu, K.-I. Jang, J. W. Lee, Z. Liu, P. Gutruf, X. Huang, P. Wei, F. Liu, K. Li, M. Dalal, R. Ghaffari, X. Feng, Y. Huang, S. Gupta, U. Paik, J. A. Rogers, *Small* **2015**, *11*, 906.

[10] S. Xu, Y. Zhang, K. E. Mathewson, K.-I. Jang, J. Kim, H. Fu, X. Huang, P. Chava, R. Wang, S. Bhole, L. Wang, Y. J. Na, Y. Guan, M. Flavin, Z. Han, Y. Huang, J. A. Rogers, *Science* **2014**, *344*, 70.

[11] A. Koh, D. Kang, Y. Xue, S. Lee, R. M. Pielak, J. Kim, T. Hwang, S. Min, A. Banks, P. Bastien, M. C. Manco, L. Wang, K. R. Ammann, K.-I. Jang, P. Won, S. Han, R. Ghaffari, U. Paik, M. J. Slepian, G. Balooch, Y. Huang, J. A. Rogers, *Sci. Transl. Med.* **2016**, *8*, 366ra165.

[12] S. Han, J. Kim, S. M. Won, Y. Ma, D. Kang, Z. Xie, K.-T. Lee, H. U. Chung, A. Banks, S. Min, S. Y. Heo, C. R. Davies, J. W. Lee, C.-H. Lee, B. H. Kim, K. Li, Y. Zhou, C. Wei, X. Feng, Y. Huang, J. A. Rogers1, *Sci. Transl. Med* **2018**, *10*, eaan4950.

[13] S. E. Gustafsson, *Rev. Sci. Instrum.* **1991**, *62*, 797.

[14] S. Krishnan, Y. Shi, R. C. Webb, Y. Ma, P. Bastien, K. E. Crawford, A. Wang, X. Feng, M. Manco, J. Kurniawan, E. Tir, Y. Huang, G. Balooch, R. M. Pielak, J. A. Rogers, *Microsyst. Nanoeng.* **2017**, *3*, 17014.

[15] R. C. Webb, A. P. Bonifas, A. Behnaz, Y. Zhang, K. J. Yu, H. Cheng, M. Shi, Z. Bian, Z. Liu, Y. S. Kim, W. H. Yeo, J. S. Park, J. Song, Y. Li, Y. Huang, A. M. Gorbach, J. A. Rogers, *Nat. Mater.* **2013**, *12*, 938.

[16] R. C. Webb, R. M. Pielak, P. Bastien, J. Ayers, J. Niittynen, J. Kurniawan, M. C. Manco, A. Lin, N. H. Cho, V. Malyrchuk, G. Balooch, J. A. V. Rogers, *PLos One* **2015**, *10*, e0118131.

[17] L. Tian, Y. Li, R. C. Webb, S. Krishnan, Z. Bian, J. Song, X. Ning, K. Crawford, J. Kurniawan, A. Bonifas, J. Ma, Y. Liu, X. Xie, J. Chen, Y. Liu, Z. Shi, T. Wu, R. Ning, D. Li, S. Sinha, D. G. Cahill, Y. Huang, J. A. Rogers, *Adv. Funct. Mater.* **2017**, *27*, 1701282.

[18] Y. Hattori, L. Falgout, W. Lee, S.-Y. Jung, E. Poon, J. W. Lee, I. Na, A. Geisler, D. Sadhwani, Y. Zhang, Y. Su, X. Wang, Z. Liu, J. Xia, H. Cheng, R. C. Webb, A. P. Bonifas, P. Won, J.-W. Jeong, K.-I. Jang, Y. M. Song, B. Nardone, M. Nodzenski, J. A. Fan, Y. Huang, D. P. West, A. S. Paller, M. Alam, W.-H. Yeo, J. A. Rogers, *Adv. Healthcare Mater.* **2014**, *3*, 1597.

[19] K. E. Crawford, Y. Ma, S. Krishnan, C. Wei, D. Capua, Y. Xue, S. Xu, Z. Xie, S. M. Won, L. Tian, C. Webb, Y. Li, X. Feng, Y. Huang, J. A. Rogers, *Extreme Mech. Lett.* **2018**, *22*, 27.

[20] S. R. Madhvapathy, Y. Ma, M. Patel, S. Krishnan, C. Wei, Y. Li, S. Xu, X. Feng, Y. Huang, J. A. Rogers, *Adv. Funct. Mater.* **2018**, *28*, 1802083.

[21] R. C. Webb, S. Krishnan, J. A. Rogers, in *Stretchable Bioelectronics for Medical Devices and Systems* (Eds: J. A. Rogers, R. Ghaffari, D.-H. Kim), Springer, Berlin **2016**, pp. 117–132.

[22] Y. Li, Y. Ma, C. Wei, H. Luan, S. Xu, M. Han, H. Zhao, C. Liang, Q. Yang, Y. Yang, K. E. Crawford, X. Feng, Y. Huang, J. A. Rogers, *Adv. Funct. Mater.* **2018**, *28*, 1801380.

[23] R. B. Belser, W. H. Hicklin, *J. Appl. Phys.* **1959**, *30*, 313.

[24] S. D. Wang, M. Li, J. Wu, D.-H. Kim, N. Lu, Y. Su, Z. Kang, Y. Huang, J. A. Rogers, *J. Appl. Mech.* **2012**, *79*, 031022.

[25] H. Chen, V. V. Ginzburg, J. Yang, Y. Yang, W. Liu, Y. Huang, L. Du, B. Chen, *Prog. Polym. Sci.* **2016**, *59*, 41.

[26] ETHZ, *Tissue Properties Database*, **2010**, http://www.itis.ethz.ch/
virtual-population/tissue-properties/database/heat-capacity/
(accessed: July 2018).

[27] Dow Corning, *Dow Corinng MG7-1010 Soft Skin Adhesive for Medical
Device Applications*, Dow Corning, Midland, MI **2016**.

[28] N. Lu, J. Yoon, Z. Suo, *Int. J. Mater. Res.* **2007**, *98*, 717.

[29] M. Hidaka, M. Matsumae, K. Ito, R. Tsugane, Y. Suzuki, *Eur. J. Nucl.
Med.* **2001**, *28*, 888.

[30] R. C. Webb, Y. Ma, S. Krishnan, Y. Li, S. Yoon, X. Guo, X. Feng,
Y. Shi, M. Seidel, N. H. Cho, J. Kurniawan, J. Ahad, N. Sheth,
J. Kim, J. G. Taylor VI, T. Darlington, K. Chang, W. Huang, J. Ayers,
A. Gruebele, R. M. Pielak, M. J. Slepian, Y. Huang, A. M. Gorbach,
J. A. Rogers, *Sci. Adv.* **2015**, *1*, e1500701.

[31] S. Verdier-Sévrain, F. Bonté, *J. Cosmet. Dermatol.* **2007**, *6*, 75.

[32] M. Takenouchi, H. Suzuki, H. Tagami, *J. Invest. Dermatol.* **1986**, *87*, 574.

[33] R. R. Warner, M. C. Myers, D. A. Taylor, *J. Invest. Dermatol.* **1988**, *90*,
218.

[34] F. Xu, T. Lu, K. Seffen, *J. Mech. Phys. Solids* **2008**, *56*, 1852.

[35] N. Tang, Z. Peng, R. Guo, M. An, X. Chen, X. Li, N. Yang, J. Zang,
Polymer **2017**, *9*, 688.

[36] E. Held, H. Lund, T. Agner, *Contact Dermatitis* **2001**, *44*, 229.

[37] B. Querleux, S. Richard, J. Bittoun, O. Jolivet, I. Idy-Peretti, R. Bazin,
J. L. Lévêque, *Skin Pharmacol. Physiol.* **1994**, *7*, 210.

[38] D. Yang, M. C. Converse, D. M. Mahvi, J. G. Webster, *IEEE Trans.
Biomed. Eng.* **2007**, *54*, 1382.

[39] C. Jin, Z. He, S. Zhang, M. Qia, Z. Sun, D. Di, J. Liu, *Infrared Phys.
Technol.* **2012**, *55*, 462.

[40] S. Weinbaum, L. X. Xu, L. Zhu, A. Ekpene, *J. Biomech. Eng.* **1997**,
119, 278.

[41] M. M. Chen, K. R. Holmes, V. Rupinskas, *J. Biomech. Eng.* **1981**,
103, 253.

[42] M. Nitzan, S. O. Anteby, Y. Mahler, *Phys. Med. Biol.* **1985**, *30*, 557.

[43] F. C. Regas, H. P. Ehrlich, *J. Trauma: Inj., Infect., Crit. Care* **1992**, *32*,
557.

[44] G. Shin, et al., *Neuron* **2017**, *93*, 509.

[45] I. H. Blank, *J. Invest. Dermatol.* **1952**, *18*, 433.